Full length article

Analysis of laser-induced microcracking in tungsten under additive manufacturing conditions: Experiment and simulation

Bey Vrancken*, Rishi K. Ganeriwala, Manyalibo J. Matthews

Lawrence Livermore National Laboratory, 7000 East Avenue, Livermore CA 94550, USA

ARTICLE INFO

ABSTRACT

Tungsten is receiving increasing interest as a plasma facing material in the ITER fusion reactor, collimators, and other structural, high temperature applications. Concurrently, there is a demand for manufacturing techniques capable of processing tungsten into the desired geometries. Additive manufacturing is a promising technique able to produce complex parts, but the structural integrity is compromised by microcracking. This work combines thermomechanical simulations with in situ high-speed video of microcracking in single laser-melted tracks, visualizing the ductile-to-brittle transition. Microcracking is shown to occur in a narrow temperature interval between 450 K–650 K, and to be strain rate dependent. The size of the crack-affected area around the scan track is determined by the maximum Von Mises residual stress, whereas crack network morphology depends on the local orientation of the principal stress. The fundamental understanding provided by this work contributes to future efforts in crack free, additively manufactured tungsten.

1. Introduction

Tungsten is a preferred material for high temperature applications due to its favorable thermomechanical properties, such as a high melting point, high thermal conductivity, and moderate thermal expansion. Additionally, its high density and extremely low sputter erosion rate make it suitable for radiation or other extreme environments, with applications ranging from waveguides and collimators, to plasma facing components (PFC) in the ITER fusion reactor [1,2]. Despite these favorable properties, the widespread use of tungsten is limited by a low thermal shock resistance and brittleness at low temperatures. For extremely demanding applications such as the PFC in ITER, the recrystallization-induced loss of strength and ductility by repeated thermal loading also needs to be addressed [3–5].

The ductile-to-brittle transition temperature or DBTT determines the lower temperature limit of the practical working range. At this temperature, the screw dislocations that could move with relative ease at higher temperatures turn immobile, leading to a sudden and drastic decrease of the ductility at lower temperatures [6]. Unfortunately, the ductile-to-brittle transition (DBT) occurs above room temperature (473 K – 673 K or higher [7–9]) and is inevitably encountered when cooling down from processing at high-temperature. At that moment, processing-induced residual stresses can lead to microcracking. The DBTT depends heavily on the interstitial impurity content, with a small increase from 10 ppm to 50 ppm oxygen impurity content increasing the DBTT from 623 K to 823 K [10]. In additive manufacturing (AM), more specifically in laser powder bed fusion (LPBF), rapid and repetitive local heating, solidification, and cooling cycles create high residual stresses that lead to distortions [11,12], cracking [13,14], and affect mechanical properties [15]. High densities larger than 98% have been reported in several AM studies of tungsten [13,16–18], but none were able to avoid the formation of microcracks [19,20].

Possible mitigation strategies have included alloying and process optimizations, with limited success in either case. For example, cracking was reduced by the addition of nanosized ZrC powder to the original tungsten powder, as the ZrC appeared to have survived exposure to the high temperature tungsten melt, leading to a 50% reduction in grain size [21]. Alloying with up to 5 wt% Ta by using powder blends has seen mixed results with no improvement observed in Ref. [16], but reduced cracking by 80% according to Ref. [22]. In the latter study, the reduction is attributed to a change in solidification mode from planar to cellular that trapped nanosized pores at the cell walls. These pores originated from boiling WO_x oxides and are thought to provide a similar strengthening effect as the nanopores in potassium doped W [23]. On the other hand, modifications of the process conditions rather than the alloy composition focused mainly on base plate preheating, with a 673 K preheated substrate not leading to significant improvements [16], though a reduction in cracking was observed when using a substrate preheated to 1273 K [17]. Using femtosecond laser pulses rather than a continuous mode laser limited the

thermally affected zone in Ref. [24], which contributed to a reduction of microcracking, though the mechanism was not discussed. For Mo, in which microcracks form due to the DBT as well, laser power/scan speed ratios $P/v < 1$ J/mm were found to reduce cracking in combination with a support structure that limited thermal conduction to the base plate [25]. Research into the thermal or mechanical properties of LPBF W is limited due to the microcracking. Nevertheless, the compressive strength at room temperature was determined to be 1253 MPa, and the thermal conductivity equal to 148 W/(m*K) [18], compared to 1432 MPa (tension) and 173 W/(m*K) for stress relieved tungsten [26].

Though it is understood by now that the DBT is the cause of microcracks in LPBF of tungsten, a fundamental understanding of their formation is still lacking, since research has been restricted to the post mortem examination of crack networks. This work utilizes in situ, high-speed video of tungsten single tracks to study in more detail the influence of the process parameters and melt geometry on the cracking mechanism by providing a visualization of the DBT. Additionally, a calibrated thermomechanical model utilizing Lawrence Livermore National Laboratory's Diablo [27] finite element code allows correlation of the cracking with residual stress, strain rate, and temperature. The results provide guidance for process parameter selection, and will act as a baseline to compare the influence of process and alloy modifications on mitigating microcracking in LPBF of W.

2. Materials & methods

2.1. High-speed video

The high-speed imaging platform is described in detail in Ref. [28], and is shown schematically in Fig. 1. A Photron SA-X2 high-speed camera coupled to high numerical optics (Mitutoyo 10x/NA0.1 microscope objective, 32 mm working distance) captures high resolution video at a 50 kHz frame rate and 768 × 328 pixel resolution, which was equivalent to a 620 × 265 μm field of view. The field of view was stationary, focused on the center of the track, and the laser scanned across the image (shown in red). Top-down vision is made possible by the dichroic longpass filter mounted above the W substrate, transparent to wavelengths > 1000 nm, but reflecting the wavelengths used for imaging to the high-speed camera (shown in green in Fig. 1). A Cavilux HF 500 W low coherence laser source (λ = 808 nm) pulsed at 1 μs provided coaxial illumination through a beamsplitter inside a Navitar Zoom 6000 system. A 1070 nm wavelength JK FL600 Yb:glass fiber laser operating in continuous wave mode with a maximum power output of 600 W was used to scan single, 2 mm long tracks on a tungsten plate. A 50 μm and 100 μm Gaussian beam diameter ($1/e^2$) were used to investigate the effect of beam spot size. 10 and 20 repetitions were performed for each parameter set utilizing a 50 μm beam and 100 μm beam, respectively. Ar was flown freely over the substrate at a rate of 0.5 l/min.
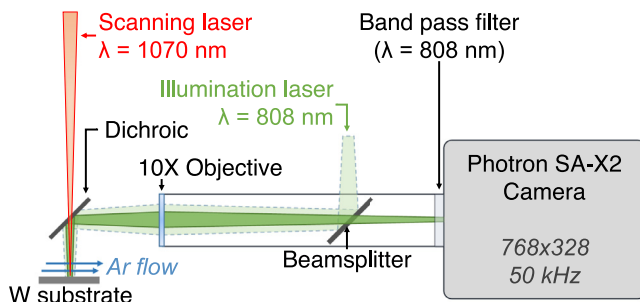

Fig. 1. Schematic of the optical setup for top down high-speed video of laser scans on a tungsten plate.

The 2 mm thick W substrates were cut from a 25.4 mm diameter, >99.95% purity W rod supplied by Eagle Alloys Corporation using wire EDM, after which the surface was partially ground using 600-grit SiO_2 paper. The oxygen content of the plate as reported by the manufacturer was 30 ppm.

2.2. Characterization

The top surface of the scan track morphology and crack-affected zone surrounding the track were examined using a Keyence VK-X100 3D laser scanning microscope, as well as the melt pool width for calibration of the thermomechanical models. The substrates were sectioned, ground, and polished using standard metallographic sample preparation techniques. The microstructure was revealed using swab etching for 5–60 s with a modified Murakami's reagent (15 g K_3Fe $(CN)_4$ + 2 g KOH dissolved in 100 ml H_2O), and examined using a FEI Quanta 200 environmental SEM.

2.3. Thermomechanical model

The implicit, Lagrangian finite element code Diablo [27], which employs distributed memory parallelism, was used to perform thermal and thermomechanical simulations of the single tracks on a tungsten substrate. Convection, radiation, and evaporation boundary conditions were included on the top surface of the model. An emissivity of 0.35 was used and a convection coefficient of 6 W/m^2-K was calculated from the experimental Ar flow conditions of laminar flow over a flat plate [29]. For both convection and radiation, a far field temperature of T_∞ = 303 K was used. The evaporation boundary condition includes the effects of latent heat of evaporation and the heat loss due to mass flux from vaporization [30]. The bottom surface of the plate was fixed at T_0 = 303 K. For the mechanical simulations, zero normal displacements were prescribed on all sides of the computational domain except the top surface. As Diablo is a Lagrangian code, fluid flow after melting is not explicitly modeled. As such, a Goldak [31] type volumetric heat source was used and the ellipsoidal dimensions were tuned to match the experimental melt pool width. Effective absorptivity values varied from 0.35 to 0.65 depending on the process parameters and were determined from experiments conducted in Ref [32]. Interpolation between the experimental absorptivity measurements was performed for process parameter settings not directly measured.

Temperature-dependent thermophysical properties (thermal conductivity, specific heat, density, coefficient of thermal expansion, and latent heats of phase change) for pure W were obtained up to melt from Refs [33,34]. Temperature-dependent mechanical and material properties (Young's modulus, yield stress, Poisson's ratio, hardening modulus) were obtained up to at least 1473 K from Appendix A of the ITER structural design criteria for in-vessel components (SDC-IC) [26]. No mechanical properties could be found at higher temperatures. As such, the yield stress was linearly extrapolated to 0 MPa at the melt temperature, such that there would be 0 deviatoric stress at temperatures greater than melt. Similarly, the Young's modulus was decreased to 10% of its room temperature value upon reaching melt. All other material properties were held constant above their reported temperature range. A finite deformation, strain rate independent material model with linear isotropic hardening was used, as described in [35]. All accumulated plastic strains were reset upon reaching the melt temperature. Further details concerning the numerical solution strategies employed by Diablo can be found in [36].

Half symmetry was used to reduce the size of the simulations. The symmetry plane was along the center of the scan track with normal vector transverse to the scan. A mesh size of 10 μm was used along the longitudinal direction (x) of the beam and 5–10 μm spacing along the transverse direction (y) within the vicinity of the melt pool. A similar mesh size was used in the z, or depth, direction. The mesh

size increased further away from the melt area. The total simulation domain was $3.5 \times 1.25 \times 2$ mm^3, which was large enough to ensure that uncertainties in the boundary conditions at the edges of the computational domain did not affect the predicted temperatures or stresses in the regions and time scales of interest. The simulations employed approximately 1 million elements and required computation times on the order of 10^3 to 10^4 cpu-hours each, based upon the process parameter settings and physics involved (thermal vs. thermomechanical). The mesh size was determined via a refinement study where using a more refined mesh did not significantly change the temperatures in the region of interest.

The ellipsoidal dimensions of the Goldak heat source were calibrated by matching the experimental melt pool width with the model melt pool width, as shown in Fig. 2a. The resulting predicted melt lengths compare well with the experimentally observed melt lengths in Fig. 2b.

3. Results

The parameter sets used in this work are shown in Fig. 3, consisting of different scan speeds v, laser power P, and laser beam diameter $\varnothing$. The linear energy input P/v covered by the parameter sets in Fig. 3 ranges between $0.6 < P/v < 6$ J/mm. Although various scaling terms have been used to normalize data presented from LPBF experiments [37,38], the results below will show that P/v achieves the most physically relevant scaling for this work. For high laser powers, longitudinal cracks along the center line of the track occurred as indicated by the red markers, which will be discussed in Section 3.2.
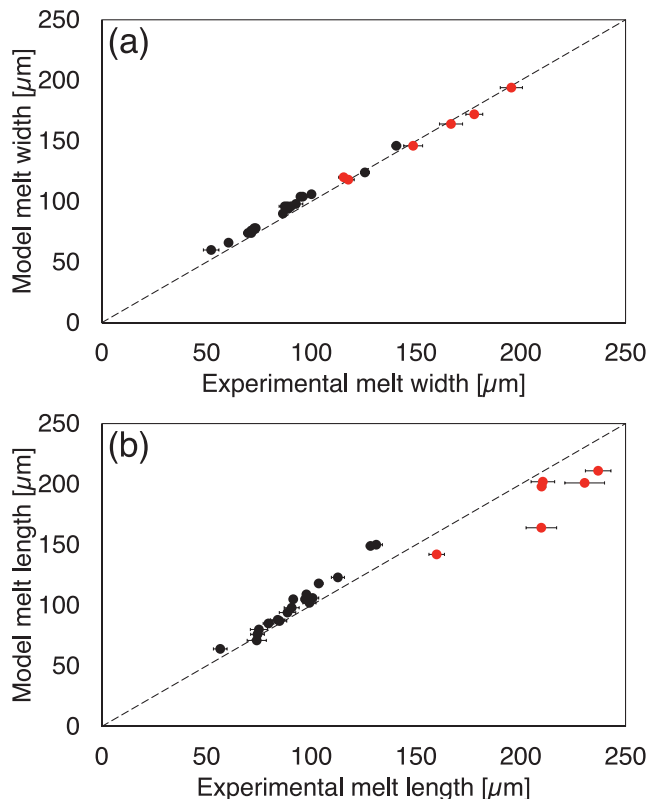
Fig. 2. Comparison of the experimentally determined (a) melt pool width, and (b) melt pool length, and the predicted width and length from the thermal model. Horizontal error bars are ± one standard deviation. The melt dimensions in the simulations were constant in the steady state regime. The red markers correspond to datasets in which longitudinal cracking was observed, which will be discussed in Section 3.1 and 3.2. (For interpretation of the references to colour in this figure legend, the reader is referred to the web version of this article.)
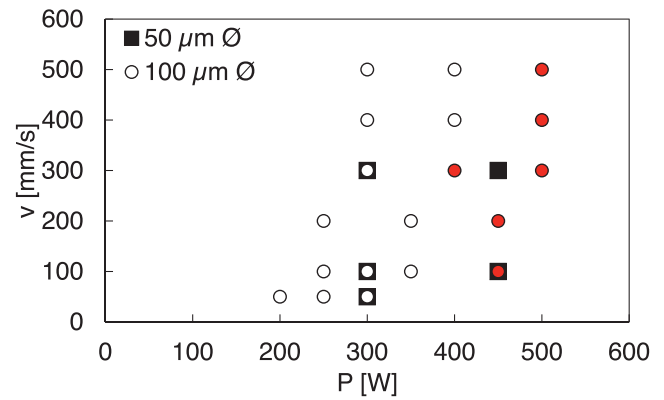
Fig. 3. Laser power P - Scan speed v − beam diameter Ø combinations used in this work. The red markers indicate parameter combinations that led to longitudinal cracking. (For interpretation of the references to colour in this figure legend, the reader is referred to the web version of this article.)

3.1. Melt pool behavior

Two representative melt pool geometries encountered in this work are shown in Fig. 4. Contrary to metal alloys such as 316 L or AlSi10Mg, W does not have a clearly defined melt pool boundary when processed by LPBF. Instead, epitaxial growth and a planar solidification front ensure there is a seamless transition between the substrate microstructure and the solidification structure, as in other pure metals like Ta [39], or alloys with a small solidification range such as Ti6Al4V [40]. In this work, the substrate microstructure consisted of elongated grains perpendicular to the surface on which the tracks were scanned, which is similar to the elongated grains that develop in the build direction during LPBF of W [16]. Therefore, the microstructure of the substrate and single scan track in this work are representative of the microstructure that develops during LPBF, and the crack paths into the substrate are similar to the vertical cracks previously encountered in LPBF of W [13].

For most of the parameter sets, the melt pool is stable and in the so-called 'conduction mode' (Fig. 4a), except the sets indicated by the red markers in Fig. 3 that led to deeper melt pools and longitudinal cracking (Fig. 4b). In Fig. 4a, the track surface is flat with minor formation of a chevron pattern, and the melt pool is shallow with depth $d = 25$ μm. The melt width w (73 ± 2 μm) is smaller than the beam diameter $\varnothing = 100$ μm, indicating that the tails of the Gaussian distributed laser power are not sufficiently powerful to heat the material above the melting point $T_m = 3695$ K. In contrast, the top surface track morphology shown in Fig. 4b is indicative of a more violent melt behavior. The power $P = 450$ W was high enough to boil the tungsten at $T_b = 6203$ K, creating a vapor depression resulting in a deeper melt with depth $d = 223$ μm. Further on, the scan track shown in Fig. 6 has a melt width $w = 116 \pm 2$ μm. Its chevron pattern is more apparent than that in Fig. 4a due to the higher laser power, yet is less unstable than in Fig. 4b. This periodic rippling of weld beads has long been observed and is attributed to different phenomena, including instability due to evaporation, thermocapillary instability, or varying solidification rates [41].

In Fig. 5, the round and square markers show an increasing melt pool width with increasing laser power. The cross-shaped markers indicate that the melt pool remains shallow (width/depth ratios $w/d > 2$) for most parameter combinations except for high laser powers $P > 400$ W, as shown in red, again corresponding to the red parameter sets in Fig. 3 for which longitudinal cracking was observed. In those cases, the melt pool is nearly as deep as it is wide, which resulted in thin, vertically oriented grains in the center of the melt pool (Fig. 4b). Applying the scaling laws derived by Rubenchik et al. [37] leads to a scan speed independent, 380 W laser power to reach the boiling temperature at 6203 K. However, experimental results by Matthews et al.
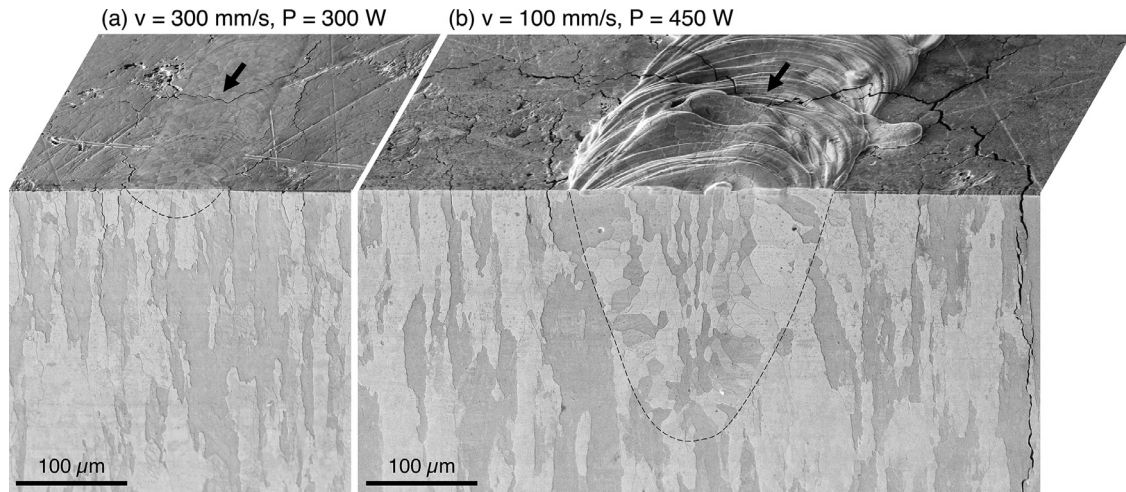
Fig. 4. Melt pool top surface and cross section for (a) P = 300 W, v = 300 mm/s, Ø = 100 μm, and (b) P = 450 W, v = 100 mm/s, Ø = 100 μm. The crack network scales with the melt pool size, which is shallow in (a) but deep in (b), leading to a deep penetration of cracks into the substrate seen on the right. The black arrows indicate transversal cracks.

[32] indicate that this threshold power increases with increasing scan speed. The threshold in this work was observed between 350 W and 400 W for v = 300 mm/s, and above 400 W for v = 400 mm/s and 500 mm/s. Boiling induces a deeper melt cavity, which in turn roughly doubles the absorptivity through multiple scattering of the laser within that cavity [32,42]. The depths of tracks created using Ø = 50 μm was not investigated, nor was it possible to distinguish the melt pool cross section from the substrate microstructure for parameter sets where P = 200 W.

3.2. Cracking behavior

The crack network around the scan track shown in Fig. 6 is representative of the crack pattern for most parameter sets. The cracks are roughly transversal across the scan vector but still adhere to grain boundaries, surrounded by a branched crack network in an area roughly 3−4 times the melt width. Moreover, the vertical crack on the right in Fig. 4b shows that cracks not only occur far away from the scan track, but also penetrate deeply into the substrate, with crack propagation facilitated by the elongated grain structure of the substrate.
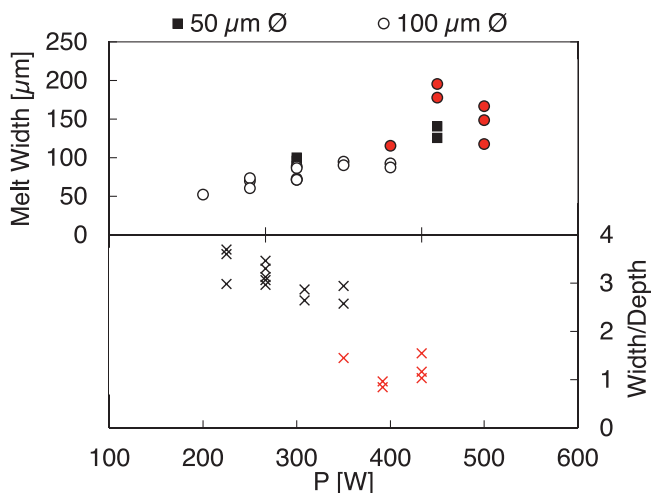

Fig. 5. Melt pool width and width-to-depth ratio as a function of laser power P. Melt pool depth data was only analyzed for Ø = 100 μm parameter sets. The red markers correspond to parameter sets for which longitudinal cracking was observed. (For interpretation of the references to colour in this figure legend, the reader is referred to the web version of this article.)

In Fig. 7, a video still shows the locations of two transversal cracks and the delay between passage of the melt pool and cracking. The full video is found in Supplementary Video 1, where a moderate amount of turbulence is visible on the melt pool top surface through the specular reflections, which contributes to the formation of the surface ripples on the solidified track. More importantly, it is evident that the two cracking events within the solidified material do not occur in the vicinity of the melt pool. Rather, there is a delay after the passage of the melt pool before a crack appears. While Supplementary Video 1 is a single example for P = 450 W, v = 300 mm/s, and Ø = 50 μm, examples for other P-v-Ø combinations are provided in the other supplementary materials (available online). As the videos are restricted to the surface, it is not clear whether the cracks initiate near the surface or within the material. Cracks traversing the scan track, which is on the order of magnitude 100 μm wide, appeared instantaneously between two frames at a 50 kHz frame rate, indicating crack growth rates of at least 5 m/s. Given that most cracks in the track are transversal, the crack spacing can be determined by the total crack count divided by the total track length. Fig. 8a shows that this crack spacing increases with increasing laser power, rising from 250 μm to 600 μm before the onset of longitudinal cracking. The longitudinal cracks partially relieve the residual stress and fewer transversal cracks are induced as a result.

In Fig. 8b, the time delay between solidification and cracking shows a linear correlation with the linear energy input P/v, which will be discussed in Section 4.1. Each data point is the median of cracking delays determined from 10 (for Ø = 50 μm) or 20 videos (for Ø = 100 μm). The median is chosen over the average to represent the asymmetry in cracking delays. Correspondingly, the error bars represent the interquartile range (IQR). The IQR is asymmetric around the median value, as there are fewer cracks at shorter delays. In the remainder of the text, the time delays and derived crack temperatures are reported as median values with error bars corresponding to the IQR. Consistent with previous plots, the red markers indicate the presence of longitudinal cracking. The red markers show that the time delays for transversal cracks to occur when longitudinal cracks are present are slightly longer than those without longitudinal cracking, though the difference is not statistically significant. While most cracks were transversal across the scan track, this longitudinal cracking occurred for higher laser powers, which coincided with a wider, but more importantly, deeper melt pool (Fig. 5). Improper width/depth ratios < 2 in welding are known to produce excessive amounts of transversal strain and unfavorable grain orientations that can lead to longitudinal cracking [43]. Fig. 4b shows that the deep melt pool shape leads to the formation of thin, vertically oriented grains in the
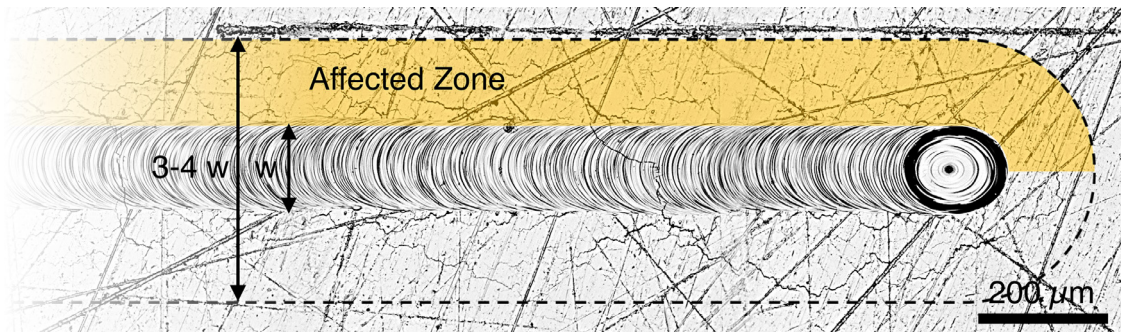
Fig. 6. Confocal image of a scan track (v = 300 mm/s, P = 400 W, Ø = 100 μm), with indication of the zone around the track in which cracks are induced.
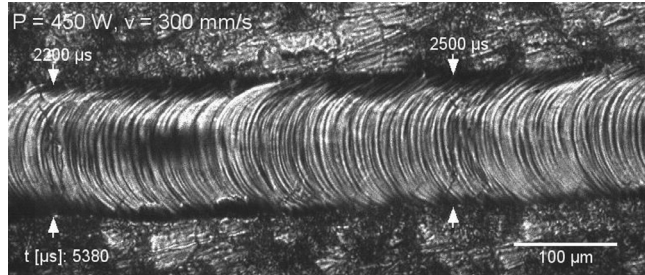
Fig. 7. Still image of the top down high speed video of a laser scan (P = 450 W, v = 300 mm/s, Ø = 50 μm) with two delayed cracking events.

middle of the solidified melt pool which provide an easy growth path for longitudinal cracks to occur.

3.3. Crack temperature

By multiplying with the scan speed, the time delay in Fig. 8b can be converted to a distance behind the trailing edge of the melt pool. In turn, this distance is used in the thermal simulations to extract the temperature at the crack location. This is illustrated in Fig. 9, showing the thermal field created by the laser traveling left to right at v = 100 mm/s, P = 450 W, and Ø = 100 μm, with the laser positioned at x = 0.9 mm. The simulated melt pool is a near perfect circle in agreement with the experiment, and the length/width ratio is small even for higher speeds due to the high thermal conductivity of W. Thermal gradients in the longitudinal direction at the solidification front exceed 3×10^7 K/m while cooling rates approach 5×10^6 K/s.

The box plot on Fig. 9 shows the median crack delay distance $\pm$ the IQR. The lines on either side extend out to the minimum and maximum

observed delays. The cracking temperature range for all parameter sets is shown in Fig. 10a as a function of P/v. Cracking consistently happened in the 450 K−650 K interval in which the DBT is expected to occur. The presence of longitudinal cracks is again indicated by the red markers. Some error bars are large and extend above the DBTT range. The large uncertainties are caused by a combination of several factors. First, the stochastic nature of material failure and in particular the location thereof, which is determined by local defects that are distributed randomly in the material. Second, it is possible that cracks initiate inside the material rather than on the surface, where the material is cooler. These cracks then propagate along the path of least resistance, which may branch into the warmer region, showing up on the surface in areas where they would not be strictly expected. Lastly, local strain rate differences can contribute as well, and will be discussed together with Fig. 10b in Section 4.2.

3.4. Crack network size and morphology

The top view of the Von Mises residual stresses after completion of the scan are shown in Fig. 11a for v = 300 mm/s, P = 300 W, and Ø = 100 μm. The inner dashed white line indicates the material that underwent melting and solidification, i.e. the scan track. The outer dashed line is an indication of the crack-affected area as described in Fig. 6, and is seen to correspond to the region in which the Von Mises stress is high. In Fig. 11b−d, the longitudinal, transversal, and Von mises stresses are shown along x = 0, scaled by the melt pool half width so that a value of 1 on the horizontal axis corresponds to the edge of the scan track (shaded in red). These stresses are shown for five distinct P/v ratios which span the range of values investigated in this work. From the line graphs in Fig. 11b−d, the longitudinal stress is over 1300 MPa and the transversal stress is smaller than 600 MPa within the scan track, whereas the transversal stress peaks around 1000 MPa adjacent to the track as the longitudinal stress falls to
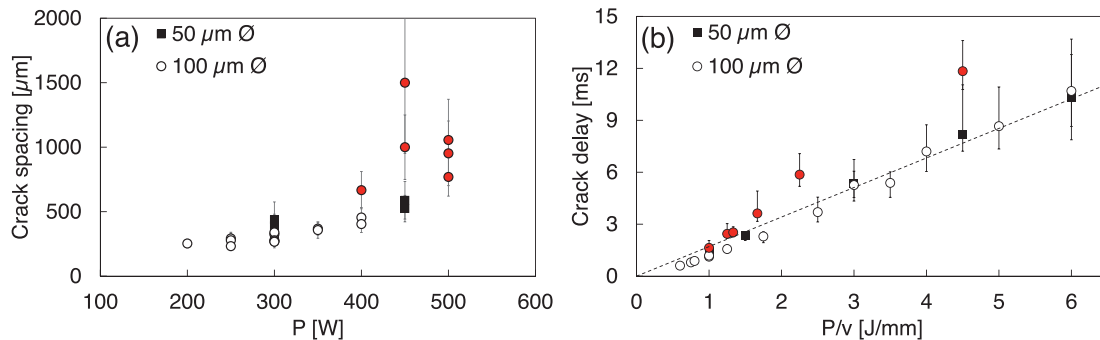
Fig. 8. (a) The crack spacing along the scan track increases with increasing laser power. Error bars correspond to $\pm$ one standard deviation. (b) Linear correlation between the linear energy input P/v and the delay between solidification and cracking (R^2 = 0.98, excluding the red markers and setting the intercept at zero according to Eq. (1) in Section 4.1). The crack delay is shown as the median values, the error bars correspond to the IQR. The red markers indicate the presence of longitudinal cracking in addition to transversal cracking. (For interpretation of the references to colour in this figure legend, the reader is referred to the web version of this article.)
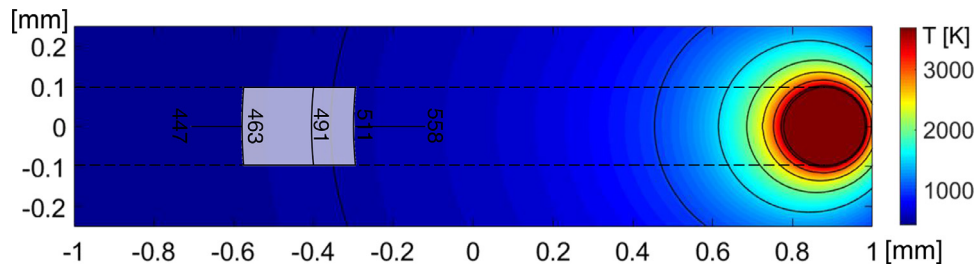
Fig. 9. Top view of Diablo thermal model of a scan track using v = 100 mm/s, P = 450 W, $\varnothing$ = 100 μm, with a boxplot indication of the temperature range at which cracking occurs.

0 MPa quickly, further away from the track. The large longitudinal stress in the scan track contributes to the transversal nature of the cracks within the track, whereas the increase in transversal stress adjacent to the track leads to the more angled, branched network of cracks in the crack-affected zone. This zone is often bounded by cracks running parallel to the scan track at roughly the location of the maximum transversal stress in Fig. 11c. There is no apparent difference in the distribution or magnitude of the transversal stress for parameters sets that displayed longitudinal cracking (see line v300-P500 indicating v = 300 mm/s and P = 500 W). This is because the discrepancy between the model and experiments is larger for cases in which boiling occurred, leading to a more turbulent, deeper melt pool. While the model does take boiling into account in the thermal balance, any associated melt pool phenomena are not captured by the model. As mentioned in Section 3.1, the deeper melt pool and vertically oriented grains assist in the formation of longitudinal cracks.

The Von Mises stress shown in Fig. 11d is relatively constant at 1300 MPa−1400 MPa in the crack-affected area but decreases quickly outside of it. The exact extent of the crack-affected zone is nondeterministic and is influenced by a combination of temperature, stress magnitude, stress orientation, local defects in the microstructure, and the occurrence of previous cracks in the vicinity that act as local stress relievers. Nevertheless, the crack-affected zone (shaded in blue in Fig. 11b-d) is roughly bounded by the region in which the Von Mises stress is higher than the yield stress, which ranges from

1000 MPa to 1150 MPa in the DBT temperature interval observed in this work [26].

4. Discussion

4.1. Cracking delay vs P/v

A Goldak heat source approximation was used in the thermomechanical model to accurately capture the melt pool shape. However, since cracks occur at a significant distance from the melt pool, in a region where temperatures are closer to T_0 than T_m, it is convenient to consider the linear correlation between the cracking time delay Δt and the linear energy input P/v using the simple Rosenthal equation [44], which utilizes a point heat source and is given by:

$$T - T_0 = \left(\frac{q/v}{2\pi k t} \right) e^{-r^2/4\alpha t} \tag{1}$$

In Eq. (1), T_0 is the surrounding equilibrium temperature, q the heat input, v the scan speed, k the thermal conductivity, α the thermal diffusivity, and r the distance from the centerline of the track. Considering the centerline ($r = 0$) and with $q = AP$, where A is the absorptivity and P the laser power, the time between solidification at T_m and reaching a certain, fixed cracking temperature T_{crack} is shown to be proportional to P/v, as shown in Eq. (2).

$$\Delta t = t_{crack} - t_m = \frac{P}{v} \left(\frac{A}{2\pi k} \right) \left(\frac{1}{T_{crack} - T_0} - \frac{1}{T_m - T_0} \right) \tag{2}$$

4.2. Strain rate dependence

Rather than a constant cracking temperature, there is a noticeable increase for lower P/v shown in Fig. 10a. To supplement the thermal model, a thermomechanical model for all 100 μm beam P-v combinations was used to determine the residual stresses and strain rates. The calculated strain rates at the crack location ranged from 0.5 s^{-1} to 6 s^{-1}, as shown in Fig. 10b. These strain rates were extracted at the location corresponding to the maximum crack temperature observed in Fig. 10a (650 K). The strain rates in other locations will differ, and will be higher closer to the melt pool. Given the dependency of the DBTT on the strain rate discussed below, this may be an additional factor in the large uncertainties in the determined cracking temperature intervals. However, possible subsurface crack initiation is likely the most significant factor.

In Refs. [45−47], the sensitivity of the DBTT to the strain rate was investigated for strain rates between 10^{-5} s^{-1} − 10^{-2} s^{-1}. The DBTT was found to display an Arrhenius-type correlation with the strain rate: $\dot{\varepsilon} = A exp(E_{DBT}/kT_{DBT})$, where A is a scaling factor, k the Boltzmann constant, and E_{DBT} the activation energy for the mechanism governing the DBT. The DBTT decreased by roughly 80−90 K in the strain rate interval investigated in literature, with a lower DBTT for lower strain rates. Using the correlation found in literature on the strain rates in this work would correspond to a 40−45 K increase of the DBTT for lower P/v ratios. The observed increase, however, is around 150 K.
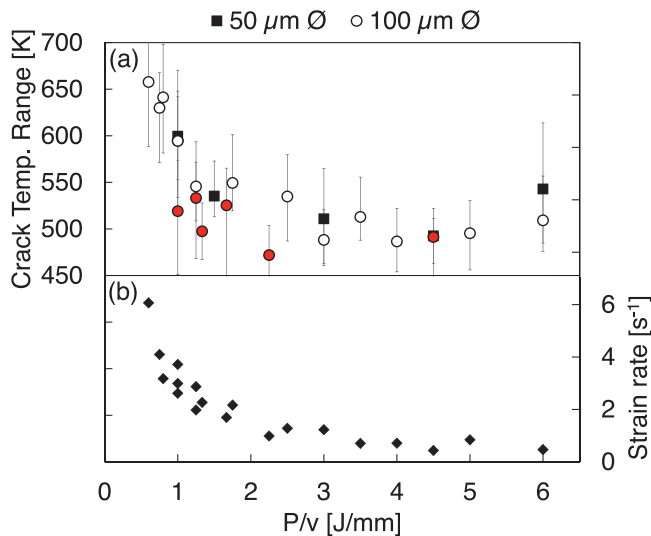

Fig. 10. (a) Temperature at the microcracking location as a function of P/v, extracted from the thermal Diablo model. (b) Strain rate for all 100 μm beam P-v combinations upon reaching 650 K (the maximum crack temperature), extracted from the thermomechanical Diablo model. The temperature markers are the median values, the error bars correspond to the IQR, which is asymmetric. The red markers correspond to parameter sets for which longitudinal cracking was observed. (For interpretation of the references to colour in this figure legend, the reader is referred to the web version of this article.)
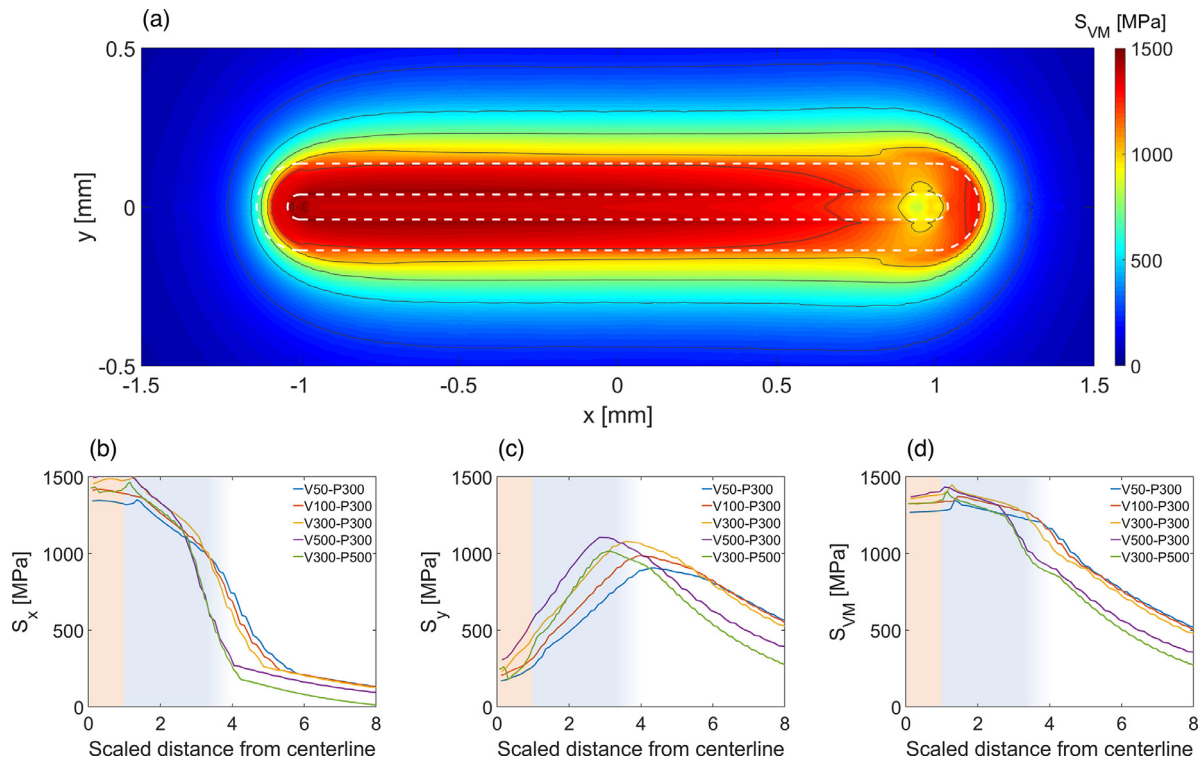
Fig. 11. (a) Top view of the Von Mises residual stress after the laser scan has completed, for v = 300 mm/s, P = 300 W and $\varnothing$ = 100 μm. The inner dashed line indicates the scan track, while the outer dashed line is a rough indication of the crack affected zone around the track. (b-d) Line graphs of the residual stress in the longitudinal direction (b), transversal direction (c), and Von Mises stress (d), as a function of normalized transverse distance, at x = 0 after cooldown. The x-axis in (b-d) is scaled by the melt width so that 1 corresponds to the edge of the scan track. The red shaded area designates the scan track, the blue shaded area the crack-affected zone. (For interpretation of the references to colour in this figure legend, the reader is referred to the web version of this article.)

An Arrhenius plot of the strain rate dependence of the DBTT in this work is given in Fig. 12, in comparison with literature data. According to Giannattasio et al. [47], the activation energy for high purity tungsten is equal to 1.0 ± 0.1 eV, while for low-purity sintered samples E_{DBT} was equal to 1.45 ± 0.12 eV, indicating that impurities not only influence the DBTT itself [10], but also its dependence on the strain rate. The work by Chilton and Wronski [45] yields E_{DBT} = 1.2 ± 1.0 eV. These values are consistent with dislocation glide of screw dislocations, partially assisted by shear stresses acting upon the dislocations [46]. Extracting an activation energy from the results of this work yields E_{DBT} = 0.32 ± 0.05 eV, evident by the shallow slope of the data from this work in Fig. 12
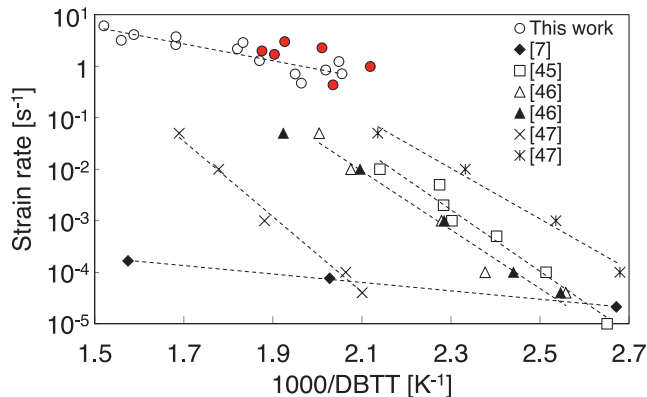
Fig. 12. Arrhenius plot of the strain rate dependence of the DBTT. Results from this work are compared to literature data [7,45–47]. Temperatures from this work are the median values. The red markers correspond to parameter sets for which longitudinal cracking was observed. (For interpretation of the references to colour in this figure legend, the reader is referred to the web version of this article.)

(R^2 = 0.79). This is considerably lower, but corresponds to the work by Gumbsch et al. [7], who derived an E_{DBT} = 0.2 eV for single crystal pure tungsten, a value consistent with edge dislocation glide (0.2–0.5 eV). This was later attributed to the orientation of the single crystal with respect to the loading, which allowed edge dislocation motion to be the governing DBT mechanism [46].

The major difference between this work and the work performed in literature to study the strain rate dependence of the DBT is the initial state of the material before the DBT is observed. In literature, the original dislocation density in the material is low, and the material is loaded in a fracture toughness test. The necessary dislocations to develop a sizeable crack tip plastic zone still need to be created, which in turn requires associated dislocations to move away from the dislocation nucleation sites. Screw dislocations are slower than edge dislocations, making the motion of the former the governing mechanism [47]. As the dislocation densities in laser powder bed fusion are known to be very high due to the thermal residual stresses [48], the dislocation density of the material in and surrounding the scan track will be substantially higher, possibly alleviating the need for motion of the associated screw dislocations, though this requires further investigation. Other factors affecting the results in this work include (i) the higher magnitude of the strain rate, (ii) microstructural differences, (iii) the continuous cooling nature of this work compared to the isothermal tests in literature, and (iv) that the strain rate and crack temperature are not controlled variables as in literature, but rather a result of thermomechanical modeling.

4.3. Crack mitigation

The main crack-reducing strategy employed in literature is preheating to a temperature above the DBTT. This research suggests that using a high P/v ratio would be beneficial, since the lower strain rates lead to a slightly lower DBTT, though the lower strain rate does not

translate to a significantly lower residual stress. However, the crack-affected area was also larger when using a high P. Literature on LPBF of Mo suggests that using $P/v < 1$ J/mm in combination with support structures that limited thermal conduction to the base plate appeared to lower DBT-driven crack densities [25]. Since the DBTT of Mo is lower than that of W, the heat buildup due to the use of the support structure sufficiently increased the temperature to work above the DBTT, which at the very least should avoid cracking during laser scanning, and delay it until the part is cooled down to room temperature. Müller et al. [17] saw a reduction in, but not an elimination of W microcracking by using preheating up to 1273 K, even though this temperature is above the DBTT. It is likely that, despite the high preheating temperature, substantial residual stresses were generated that led to cracking while the part was cooled down to room temperature after the build had completed.

In addition to the influence of process parameters, the alloy composition, and more specifically the concentration of impurities, has a major effect on the cracking behavior. The atmosphere control in this work was suboptimal but unavoidable to allow in situ high speed imaging. In commercial LPBF machines, the oxygen level in the process chamber can be controlled down to 10 ppm and lower. In that case, the impurities in the powder feedstock will become a major issue. While the bar feedstock in this work contained relatively little oxygen (30 ppm), spheroidization of tungsten powders leads to an increase in impurity content. According to Tekna [49], their commercially available spherical tungsten powders in the $15-45$ μm size range contain up to 250 ppm oxygen. Similarly, 30 μm diameter, spheroidized tungsten powders manufactured at Lawrence Livermore National Laboratory contained 370 ppm. If high oxygen concentrations in the feedstock material cannot be avoided, the process may need to be adapted to actively remove impurities during processing, for example by using a hydrogen atmosphere that could act as an oxygen getter, or by small alloy additions of an element with a higher affinity for oxygen than tungsten [50].

The results in this work confirm that even though cracks occur at the microscale, mitigating the problem requires a universal strategy rather than a localized one. The time delays at which cracking occurs are too short (≤ 10 ms) for adjusted scan strategies to affect local temperature and stress distributions, and even if they were long enough, the fundamental cracking mechanism remains active. Furthermore, the crack-affected area is much larger than the scan track itself, as evidenced by Fig. 4b. Overall, this means a global rather than a local solution to the microcracking in W during LPBF is needed that affects either or both crack driving mechanisms: the residual stress and the ductile-to-brittle transition. Alloying can lower the DBTT and cause grain boundary strengthening that impedes crack growth, while base plate preheating or in situ diode annealing [51] will lower thermal gradients and raise the working temperature above the DBTT. The diagnostic tools developed in this study will be used in future work to study the influence of both alloying and preheating on microcracking in W.

5. Conclusion

For the first time, the ductile-to-brittle transition (DBT) in tungsten was directly visualized through a combined approach of thermo-mechanical modeling and in situ high speed video of microcracking during laser melting. The linear correlation of the cracking time delay after solidification and the linear energy input P/v is supported by the analytical Rosenthal equation, and translates to a cracking temperature between 450 K$-$650 K for all P-v combinations, consistent with the expected range of the DBT temperature. Furthermore, an increase of the cracking temperature for low P/v ratios was linked with an increasing strain rate, and evidence suggests edge dislocation glide to be the governing mechanism. The size of the crack-affected zone around the scan track corresponds to areas in which the maximum

Von Mises residual stress exceeded the material yield stress, while the local orientation of cracks depends on the local longitudinal and transverse components of the residual stress. This work uncovered the fundamental cracking mechanisms of tungsten in AM processing conditions. The results can serve as a baseline for future efforts in eliminating microcracking during AM of tungsten.

Declaration of Competing Interest

The authors declare that they have no known competing financial interests or personal relationships that could have appeared to influence the work reported in this paper.

Acknowledgements

Supplementary materials

Supplementary material associated with this article can be found in the online version at doi:10.1016/j.actamat.2020.04.060.

References

[1] T. Hirai, S. Panayotis, V. Barabash, C. Amzallag, F. Escourbiac, A. Durocher, M. Merola, J. Linke, T. Loewenhoff, G. Pintsuk, M. Wirtz, I. Uytdenhouwen, Use of tungsten material for the ITER divertor, Nucl. Mater. Energy 9 (2016) 616–622, doi: 10.1016/j.nme.2016.07.003.

[2] K. Deprez, S. Vandenberghe, K. Van Audenhaege, J. Van Vaerenbergh, R. Van Holen, Rapid additive manufacturing of MR compatible multipinhole collimators with selective laser melting of tungsten powder, Med. Phys. 40 (2013) 012501, doi: 10.1118/1.4769122.

[3] J. Hohe, P. Gumbsch, On the potential of tungsten$-$vanadium composites for high temperature application with wide-range thermal operation window, J. Nucl. Mater. 400 (2010) 218–231, doi: 10.1016/j.jnucmat.2010.03.007.

[4] K. Tsuchida, T. Miyazawa, A. Hasegawa, S. Nogami, M. Fukuda, Recrystallization behavior of hot-rolled pure tungsten and its alloy plates during high-temperature annealing, Nucl. Mater. Energy 15 (2018) 158–163, doi: 10.1016/j.nme.2018.04.004.

[5] T. Hirai, G. Pintsuk, Thermo-mechanical calculations on operation temperature limits of tungsten as plasma facing material, Fusion Eng. Des. 82 (2007) 389–393, doi: 10.1016/j.fusengdes.2007.03.032.

[6] P. Gumbsch, Brittle fracture and the brittle-to-ductile transition of tungsten, J. Nucl. Mater. 323 (2003) 304–312, doi: 10.1016/j.jnucmat.2003.08.009.

[7] P. Gumbsch, J. Riedle, A. Hartmaier, H.F. Fischmeister, Controlling Factors for the Brittle-to-Ductile Transition in Tungsten Single Crystals, Science 282 (1998) 1293–1295, doi: 10.1126/science.282.5392.1293.

[8] S. Antusch, D.E.J. Armstrong, T.B. Britton, L. Commin, J.S.K.-L. Gibson, H. Greuner, J. Hoffmann, W. Knabl, G. Pintsuk, M. Rieth, S.G. Roberts, T. Weingaertner, Mechanical and microstructural investigations of tungsten and doped tungsten materials produced via powder injection molding, Nucl. Mater. Energy. 3$-$4 (2015) 22–31, doi: 10.1016/j.nme.2015.04.002.

[9] R.I. Jaffee, G.T. Hahn, Structural Considerations in Developing Refractory Metal Alloys, (1963) 37.

[10] J.R. Stephens, Effects of Interstitial Impurities On the Low-Temperature Tensile Properties of Tungsten, Lewis Research Center, National Aeronautics and Space Administration, Cleveland OH, 1964 http://www.dtic.mil/docs/citations/ADA396979 .

[11] J.-.P. Kruth, J. Deckers, E. Yasa, R. Wauthle, Assessing and comparing influencing factors of residual stresses in selective laser melting using a novel analysis method, Proc. Inst. Mech. Eng. Part B J. Eng. Manuf. 226 (2012) 980–991, doi: 10.1177/0954405412437085.

[12] D. Buchbinder, W. Meiners, N. Pirch, K. Wissenbach, J. Schrage, Investigation on reducing distortion by preheating during manufacture of aluminum components using selective laser melting, J. Laser Appl. 26 (2013) 012004, doi: 10.2351/1.4828755.

[13] B. Vrancken, R. Wauthle, J.-.P. Kruth, J. Van Humbeeck, Study of the influence of material properties on residual stress in selective laser melting, in: Proceedings of the Solid Freedom Fabric Symposium, University of Texas at Austin, Austin, TX, 2013, pp. 393–407.

[14] L.N. Carter, C. Martin, P.J. Withers, M.M. Attallah, The influence of the laser scan strategy on grain structure and cracking behaviour in SLM powder-bed fabricated

nickel superalloy, J. Alloys Compd. 615 (2014) 338–347, doi: 10.1016/j.jall-com.2014.06.172.

[15] B. Vrancken, V. Cain, R. Knutsen, J. Van Humbeeck, Residual stress via the contour method in compact tension specimens produced via selective laser melting, Scr. Mater. 87 (2014) 29–32, doi: 10.1016/j.scriptamat.2014.05.016.

[16] A. Iveković, N. Omidvari, B. Vrancken, K. Lietaert, L. Thijs, K. Vanmeensel, J. Vleugels, J.-.P. Kruth, Selective laser melting of tungsten and tungsten alloys, Int. J. Refract. Met. Hard Mater. 72 (2018) 27–32, doi: 10.1016/j.ijrmhm.2017.12.005.

[17] A.V. Muller, G. Schlick, R. Neu, C. Anstatt, T. Klimkait, J. Lee, B. Pascher, M. Schmitt, C. Seidel, Additive manufacturing of pure tungsten by means of selective laser beam melting with substrate preheating temperatures up to 1000 ∘C, Nucl. Mater. Energy. 19 (2019) 184–188, doi: 10.1016/j.nme.2019.02.034.

[18] S. Wen, C. Wang, Y. Zhou, L. Duan, Q. Wei, S. Yang, Y. Shi, High-density tungsten fabricated by selective laser melting: densification, microstructure, mechanical and thermal performance, Opt. Laser Technol. 116 (2019) 128–138, doi: 10.1016/j.optlastec.2019.03.018.

[19] P. Rindt, J.M. González, P. Hoogerhuis, P. van den Bosch, M. van Maris, D. Terentyev, C. Yin, M. Wirtz, N.J.L. Cardozo, J.A.W. van Dommelen, T.W. Morgan, Using 3D-printed tungsten to optimize liquid metal divertor targets for flow and thermal stresses, Nucl. Fusion. (2019), doi: 10.1088/1741-4326/ab0a76.

[20] B. Vrancken, W.E. King, M.J. Matthews, In-situ characterization of tungsten micro-cracking in selective laser melting, Procedia CIRP 74 (2018) 107–110, doi: 10.1016/j.procir.2018.08.050.

[21] K. Li, D. Wang, L. Xing, Y. Wang, C. Yu, J. Chen, T. Zhang, J. Ma, W. Liu, Z. Shen, Crack suppression in additively manufactured tungsten by introducing second-ary-phase nanoparticles into the matrix, Int. J. Refract. Met. Hard Mater. (2018), doi: 10.1016/j.ijrmhm.2018.11.013.

[22] D. Wang, Z. Wang, K. Li, J. Ma, W. Liu, Z. Shen, Cracking in laser additively manu-factured W: initiation mechanism and a suppression approach by alloying, Mater. Des. 162 (2019) 384–393, doi: 10.1016/j.matdes.2018.12.010.

[23] B. Huang, Y. Xiao, B. He, J. Yang, J. Liao, Y. Yang, N. Liu, Y. Lian, X. Liu, J. Tang, Effect of potassium doping on the thermal shock behavior of tungsten, Int. J. Refract. Met. Hard Mater. 51 (2015) 19–24, doi: 10.1016/j.ijrmhm.2015.02.001.

[24] S. Bai, J. Liu, P. Yang, M. Zhai, H. Huang, L.-.M. Yang, Femtosecond Fiber Laser Additive Manufacturing of Tungsten, in: Proceedings of the SPIE Photonics West 9738-24, San Francisco, 2016.

[25] D. Wang, C. Yu, J. Ma, W. Liu, Z. Shen, Densification and crack suppression in selec-tive laser melting of pure molybdenum, Mater. Des. 129 (2017) 44–52, doi: 10.1016/j.matdes.2017.04.094.

[26] Appendix A to ITER SDC-IC, 2013.

[27] J.M. Solberg, N.E. Hodge, M.A. Puso, S.T. Castonguay, R.K. Ganeriwala, R.M. Ferencz, Diablo: A Parallel, Implicit Multi-Physics Finite Element Code for Engineering Anal-ysis User Manual, Lawrence Livermore National Laboratory, 2018.

[28] S. Ly, A.M. Rubenchik, S.A. Khairallah, G. Guss, M.J. Matthews, Metal vapor micro-jet controls material redistribution in laser powder bed fusion additive manufacturing, Sci. Rep. 7 (2017) 4085, doi: 10.1038/s41598-017-04237-z.

[29] F.P. Incropera, Fundamentals of Heat and Mass Transfer, John Wiley, 2007.

[30] J. Barrett, C. Clement, Kinetic evaporation and condensation rates and their coeffi-cients, J. Colloid Interface Sci. 150 (1992) 352–364, doi: 10.1016/0021-9797(92)90205-Z.

[31] J. Goldak, A. Chakravarti, M. Bibby, A new finite element model for welding heat sources, Metall. Trans. B. 15 (1984) 299–305, doi: 10.1007/BF02667333.

[32] M. Matthews, J. Trapp, G. Guss, A. Rubenchik, Direct measurements of laser absorptivity during metal melt pool formation associated with powder bed fusion additive manufacturing processes, J. Laser Appl. 30 (2018) 032302, doi: 10.2351/1.5040636.

[33] P. Tolias, Analytical expressions for thermophysical properties of solid and liquid tungsten relevant for fusion applications, Nucl. Mater. Energy 13 (2017) 42–57, doi: 10.1016/j.nme.2017.08.002.

[34] J.J. Valencia, P.N. Quested, Thermophysical Properties, ASM Handbook Vol. 15 Cast., ASM International, 2008, pp. 468–481, doi: 10.1361/asmhba0005240.

[35] R.K. Ganeriwala, M. Strantza, W.E. King, B. Clausen, T.Q. Phan, L.E. Levine, D.W. Brown, N.E. Hodge, Evaluation of a thermomechanical model for prediction of residual stress during laser powder bed fusion of Ti-6Al-4V, Addit. Manuf. 27 (2019) 489–502, doi: 10.1016/j.addma.2019.03.034.

[36] N.E. Hodge, R.M. Ferencz, J.M. Solberg, Implementation of a thermomechanical model for the simulation of selective laser melting, Comput. Mech. 54 (2014) 33–51, doi: 10.1007/s00466-014-1024-2.

[37] A.M. Rubenchik, W.E. King, S. Wu, Scaling laws for the additive manufacturing, J. Mater. Process. Technol.(n.d.). 10.1016/j.jmatprotec.2018.02.034.

[38] K. Wei, M. Gao, Z. Wang, X. Zeng, Effect of energy input on formability, micro-structure and mechanical properties of selective laser melted AZ91D magnesium alloy, Mater. Sci. Eng. A. 611 (2014) 212–222, doi: 10.1016/j.msea.2014.05.092.

[39] L. Thijs, M.L. Montero Sistiage, R. Wauthle, Q. Xie, J.-.P. Kruth, J. Van Humbeeck, Strong morphological and crystallographic texture and resulting yield strength anisotropy in selective laser melted tantalum, Acta Mater. 61 (2013) 4657–4668, doi: 10.1016/j.actamat.2013.04.036.

[40] B. Vrancken, L. Thijs, J.-.P. Kruth, J. Van Humbeeck, Microstructure and mechanical properties of a novel β titanium metallic composite by selective laser melting, Acta Mater. 68 (2014) 150–158, doi: 10.1016/j.actamat.2014.01.018.

[41] P.S. Wei, The Physics of Weld Bead Defects, in: weld, Process (2012) https://www.intechopen.com/books/welding-processes/the-physics-of-weld-bead-defects .

[42] J. Ye, S.A. Khairallah, A.M. Rubenchik, M.F. Crumb, G. Guss, J. Belak, M.J. Matthews, Energy Coupling Mechanisms and Scaling Behavior Associated with Laser Powder Bed Fusion Additive Manufacturing, Adv. Eng. Mater. 21 (2019) 1900185, doi: 10.1002/adem.201900185.

[43] S. Kou, Weld Metal Solidification Cracking, Weld. Metall., 2002, pp. 263–300 https://onlinelibrary.wiley.com/doi/10.1002/0471434027.ch11 .

[44] D. Rosenthal, The theory of moving sources of heat and its application to metal treatments, Trans. Am. Soc. Mech. Eng. 43 (1946) 849–866.

[45] A.C. Chilton, A.S. Wronski, The effects of strain rate and pressurization on the duc-tile-brittle transition temperature of polycrystalline sintered tungsten, J. Common Met. 17 (1969) 447–450, doi: 10.1016/0022-5088(69)90071-X.

[46] A. Giannattasio, S.G. Roberts, Strain-rate dependence of the brittle-to-ductile transition temperature in tungsten, Philos. Mag. 87 (2007) 2589–2598, doi: 10.1080/14786430701253197.

[47] A. Giannattasio, Z. Yao, E. Tarleton, S.G. Roberts, Brittle−ductile transitions in polycrystalline tungsten, Philos. Mag. (2010) https://www.tandfonline.com/doi/abs/10.1080/14786435.2010.502145 .

[48] Y.M. Wang, T. Voisin, J.T. McKeown, J. Ye, N.P. Calta, Z. Li, Z. Zeng, Y. Zhang, W. Chen, T.T. Roehling, R.T. Ott, M.K. Santala, P.J. Depond, M.J. Matthews, A.V. Hamza, T. Zhu, Additively manufactured hierarchical stainless steels with high strength and ductility, Nat. Mater. 17 (2018) 63–71, doi: 10.1038/nmat5021.

[49] Tekna Advanced Materials, W -45 Spherical Tungsten Powder Brochure, (n.d.). http://www.tekna.com (Accessed 20 December 2019).

[50] K. Li, G. Ma, L. Xing, Y. Wang, C. Yu, J. Chen, J. Ma, G. Wu, W. Liu, Z. Shen, X. Huang, Crack suppression via in-situ oxidation in additively manufactured W-Ta alloy, Mater. Lett. 263 (2020) 127212, doi: 10.1016/j.matlet.2019.127212.

[51] J.D. Roehling, W.L. Smith, T.T. Roehling, B. Vrancken, G.M. Guss, J.T. McKeown, M.R. Hill, M.J. Matthews, Reducing residual stress by selective large-area diode surface heating during laser powder bed fusion additive manufacturing, Addit. Manuf. 28 (2019) 228–235, doi: 10.1016/j.addma.2019.05.009.